Soft Matter

PAPER

View Article Online
View Journal | View Issue

Cite this: *Soft Matter*, 2023, **19**, 5772

Soft, flexible pressure sensors for pressure monitoring under large hydrostatic pressure and harsh ocean environments†

Yi Li,‡[a] Andres Villada,‡[b] Shao-Hao Lu,[a] He Sun,[c] Jianliang Xiao*[b] and Xueju Wang *[ad]

Traditional rigid ocean pressure sensors typically require protection from bulky pressure chambers and complex seals to survive the large hydrostatic pressure and harsh ocean environment. Here, we introduce soft, flexible pressure sensors that can eliminate such a need and measure a wide range of hydrostatic pressures (0.1 MPa to 15 MPa) in environments that mimic the ocean, achieving small size, high flexibility, and potentially low power consumption. The sensors are fabricated from lithographically patterned gold thin films (100 nm thick) encapsulated with a soft Parylene C film and tested in a customized pressure vessel under well-controlled pressure and temperature conditions. Using a rectangular pressure sensor as an example, the resistance of the sensor is found to decrease linearly with the increase of the hydrostatic pressure from 0.1 MPa to 15 MPa. Finite element analysis (FEA) reveals the strain distributions in the pressure sensor under hydrostatic pressures of up to 15 MPa. The effect of geometry on sensor performance is also studied, and radially symmetric pressure sensors (like circular and spike-shaped) are shown to have more uniform strain distributions under large hydrostatic pressures and, therefore, have a potentially enhanced pressure measurement range. Pressure sensors of all geometries show high consistency and negligible hysteresis over 15 cyclic tests. In addition, the sensors exhibit excellent flexibility and operate reliably under a hydrostatic pressure of 10 MPa for up to 70 days. The developed soft pressure sensors are promising for integration with many platforms including animal tags, diver equipment, and soft underwater robotics.

Received 29th April 2023,
Accepted 21st June 2023

DOI: 10.1039/d3sm00563a

rsc.li/soft-matter-journal

1. Introduction

With the rapid development of sensing technologies, pressure sensors have been used in many fields including health monitoring,[1–3] ocean exploring robots[4–6] and ocean animal tags.[7–9] For example, pressure sensors in conductivity–temperature–depth (CTD) sensor systems are used to monitor parameters like ocean depth and water velocity[10–14] in the ocean, which usually requires the sensor to withstand a large hydrostatic pressure. Traditional ocean pressure sensors such as those in cable-controlled underwater vehicles[15,16] and rigid underwater robots[6,17,18] are made of rigid materials, which often need the protection from a pressure chamber to survive the large hydrostatic pressure in the ocean, limiting the flexibility of the sensing systems for integration with many platforms and increasing the size and energy consumption of the sensor system.[19,20]

In the past decade, many flexible pressure sensors have been developed based on soft materials including conductive polydimethylsiloxane (PDMS) composites,[21,22] hydrogels,[23–25] liquid crystal polymers (LCPs),[26,27] and dielectric elastomers.[28,29] The flexible pressure sensors based on soft materials are promising for deep ocean sensing because of their incompressibility under large hydrostatic pressures and, therefore, the potential for eliminating pressure chambers. However, the study on the measurement range of these flexible pressure sensors so far has been mostly limited to the order of a few kPa, rarely reaching the range of MPa.[28,30–32] For example, a pressure sensor with microstructured rubber dielectric layers for electronic skin measures pressures on the order of tens of kPa.[28] More recently, a porous PDMS-based flexible pressure sensor for autonomous

[a] *Department of Materials Science and Engineering, University of Connecticut, Storrs, CT 06269, USA. E-mail: xueju.wang@uconn.edu*
[b] *Department of Mechanical engineering, University of Colorado, Boulder, CO 80309, USA. E-mail: jianliang.xiao@colorado.edu*
[c] *Department of Biomedical Engineering, University of Connecticut, Storrs, CT 06269, USA*
[d] *Institute of Materials Science, University of Connecticut, Storrs, CT 06269, USA*

† Electronic supplementary information (ESI) available: Additional experimental details, materials, and methods, including photographs of the experimental setup and results (PDF). See DOI: https://doi.org/10.1039/d3sm00563a

‡ Yi Li and Andres Villada contributed equally to this paper.

underwater vehicles is reported with a pressure measurement range of 0–230 kPa.[32] To further expand the potential applications of flexible electronics to a deep ocean environment, the desired sensors are expected to have robust performance over a wide range of hydrostatic pressures (*e.g.*, on the order of a few or tens of MPa).[33,34] For example, in our previous studies,[33,34] we introduced soft, pressure-tolerant temperature and salinity sensors with high flexibility for operating under a large hydrostatic pressure (0.1–15 MPa) and high salinity (30–40 Practical Salinity Unit (PSU)) environments, thus eliminating the need for protection from pressure chambers and potentially achieving small sensor size and low power consumption.

Here, we develop soft, flexible pressure sensors that can measure large hydrostatic pressures of up to 15 MPa *via* an integrated experimental and computational approach. The pressure sensor consists of an ultra-thin gold (Au) film encapsulated with soft polyimide (PI) and Parylene C films for depth measurements in marine environments. Pressure sensors with three types of geometries (rectangular, circular, and spike) are designed and tested in a custom-built pressure vessel to mimic the ocean environment. The resistance change of the pressure sensors is linearly proportional to the change of hydrostatic pressures (0.1–15 MPa), which shows good consistency with the simulation results *via* finite element analysis (FEA). In addition, the radially symmetric geometry (circular- and spike-shaped pressure sensors) can alleviate stress concentrations under large hydrostatic pressure, thereby improving the sensitivity and measurement range of the sensor. The pressure sensors exhibit excellent cyclic loading behaviors under varying hydrostatic pressure of 0.1–15 MPa and negligible hysteresis. In addition, they show insensitivity to bending curvatures of 0–6.18 m^{-1}, and present high stability during cyclic bending tests (1000 cycles), demonstrating high flexibility. Furthermore, sensors encapsulated with transparent Parylene C[35–37] films are shown to survive the 10 MPa pressure environment for more than 70 days, demonstrating excellent encapsulation capability under large hydrostatic pressure and harsh environments.

2. Results and discussion

2.1 Design and fabrication of soft pressure sensors for ocean sensing

The schematic illustration in Fig. 1A presents the basic idea of the developed soft pressure sensors that can be conformally integrated with various platforms at different depths of the ocean, such as divers for health monitoring (0–50 m), and marine animals like octopuses and sharks (0–1 km) to track their behaviors. The pressure sensor consists of a thin gold layer (Au, 100 nm thick)[38] prepared *via* magnetron sputtering (AJA Orion-8 Magnetron Sputtering System, AJA International Inc.) of Au onto a PI (4 μm thick) substrate, with a thin adhesion layer of chromium (Cr, 10 nm thick) between Au and PI (Fig. 1B). The Au/Cr thin film is subsequently patterned into narrow traces (42 μm wide) in serpentine geometry *via* photolithography to enhance its stretchability. To encapsulate

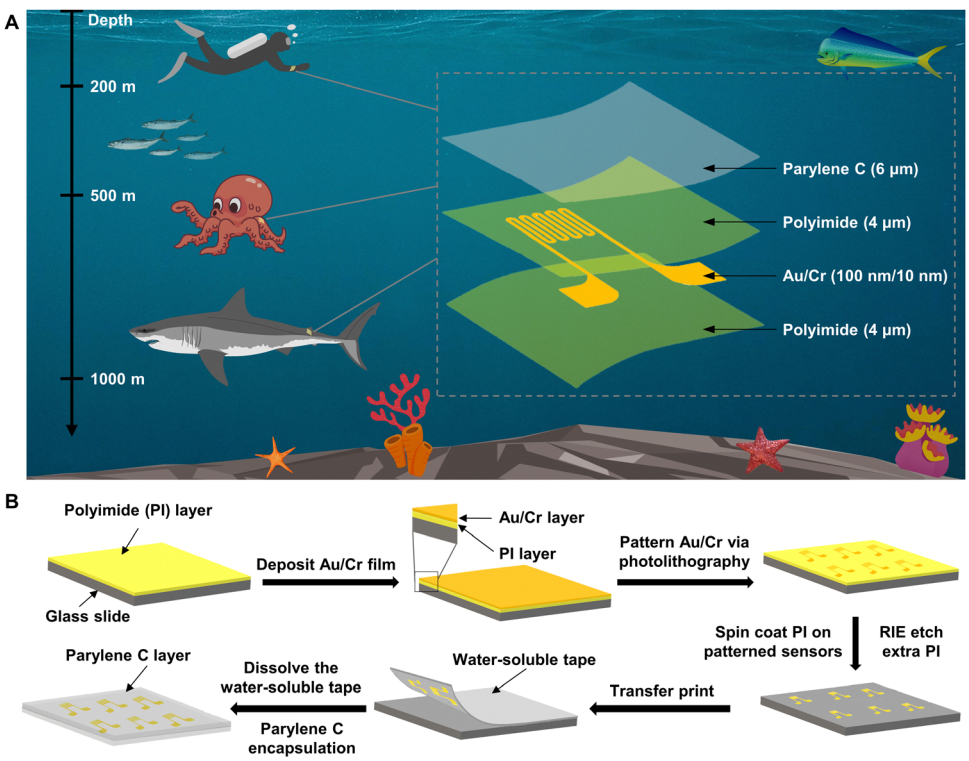

Fig. 1 Schematic illustration of (A) soft pressure sensors for integration with diverse platforms for applications in the ocean environment, and (B) the fabrication scheme of soft pressure sensors.

the Au conductive traces, another PI layer (4 μm thick) is deposited on top of Au, followed by the encapsulation with a Parylene C layer (6 μm thick, Specialty Coating Systems Inc.). The thin Parylene C coating (see details in the Experimental section) provides a number of useful properties including excellent water and ion barrier properties and biocompatibility, and, therefore, serves as an excellent encapsulation layer for pressure sensors to operate in the harsh ocean environment.[39–41] The effective modulus of this multi-layer sensor is evaluated to be 3.66 GPa (Table S1 and Supplementary Note 1), which is comparable to that of typical polymers like polyimide[42–44] and SU-8.[45–47]

2.2 Characterization and testing of the soft pressure sensor

Fig. 2A shows that the pressure sensor integrated onto a PDMS substrate is bent by two hands, exhibiting great flexibility. The zoomed-in optical microscope image demonstrates the high transparency of the Parylene C encapsulation layer, which allows monitoring of the sensor morphology during operation as well as before and after testing. To evaluate the performance of the sensor under a large hydrostatic pressure, we test the sensor in a customized pressure vessel (maximum pressure: 3000 psi; Pharr Instrument Company, Moline, IL) in the hydrostatic pressure range of 0.1–15 MPa, corresponding to an ocean depth of 0–1.5 km. Meanwhile, a three-dimensional (3D) finite element model of the pressure sensor is created using Abaqus software (Dassault Systèmes) (see details in the Experimental section) to predict the strain distribution within the sensor under hydrostatic pressures. The model uses compressive stress/strain data input to capture the elastic response of Parylene C to large compressive forces. The encapsulation layer, Parylene C, is modeled as 3D, hybrid, reduced integration elements while the other layers that comprise the sensor are modeled as shells to simplify the contact between interfaces at small strains, with various sensor layers assigned to their respective material properties and thicknesses (see Table S1, ESI†). The properties of the Au layer are assumed to be those of a thin nanocrystalline Au film with a grain size of 40 nm.[48,49] The bottom of the device is prevented from being displaced by an encastre boundary condition to model the sensor being adhered with no slipping on a rigid surface, and a hydrostatic pressure of up to 15 MPa is applied on the remaining surfaces of the device.

Fig. 2B shows that the fractional resistance change of the pressure sensor decreases linearly from 0% to −0.568% as the hydrostatic pressure increases from 0.1 MPa to 15 MPa in experiments. It should be noted that R_0 is the resistance of the pressure sensor at 0.1 MPa, and ΔR represents the difference between the resistance value (R) of the sensor and R_0. The modeling (blue curve) and experimental (black curve) results agree well. Fig. 2C and Fig. S1 (ESI†) show the predicted strain distribution within the sensor under a hydrostatic pressure of 1–15 MPa *via* FEA simulations. We can see that the strain distribution is relatively uniform under low hydrostatic pressures (1–3 MPa), but the strain distribution under high pressure levels shows that the strain starts to concentrate on certain Au traces as the pressure increases due to the out-of-plane deformation of the sensor under hydrostatic compression.

We further test the cyclic loading behavior of the sensor under hydrostatic pressure levels of 0.1 MPa–15 MPa. It can be seen that the sensor exhibits negligible hysteresis during loading and unloading, with no visible changes in the morphology of the sensor as shown in the insets of Fig. 2D. The reliability and repeatability of the sensor are further demonstrated in additional cyclic loading/unloading tests (15 cycles) (Fig. 2E and Fig. S2, ESI†), where the sensor functions well with no visible morphology changes after the cyclic testing. In addition, to quantitatively evaluate the flexibility of the pressure sensor, we conformally laminate the sensor onto 3D printed arched molds made of digital ABS (Form 3+ SLA 3D printer) and record the resistance change of the sensor under various bending curvatures of 0–6.18 m^{-1}. Fig. 2F shows that the resistance of the pressure sensor is insensitive to the curvature change, with high repeatability (standard deviation s = 0.038%; n = 3). Here, R_0 is the resistance of the pressure sensor in a flat state (zero curvature), and ΔR represents the difference between the resistance value (R) of the sensor and R_0. Furthermore, we perform the cyclic bending test (CellScale, Univert; at a loading rate of 0.5 mm s^{-1} at room temperature) of the sensor. As shown in Fig. 2G, the sensor shows high reliability with negligible hysteresis resistance changes of up to 0.0371% over 1000 cycles of bending tests. Here, similarly, R_0 is the resistance of the pressure sensor before the cyclic bending test (under zero loading).

2.3 Effect of geometry on the performance of pressure sensors

The non-uniform strain distribution in the rectangular pressure sensor under large hydrostatic pressures discussed above may lead to plastic deformation in the strain-concentrated region and, therefore, limit the pressure measurement range of the sensor. To explore the effect of geometry designs on the performance of pressure sensors, we further fabricate pressure sensors in two radially symmetric geometries: circular and spike shapes. Firstly, we design and fabricate a circular pressure sensor that consists of narrow Au traces (with the same width as that of a rectangular pattern) following the experimental procedure described in section 2.1 to reduce sharp corners and avoid stress concentrations. Fig. 3A shows that the fractional resistance change of the circular pressure sensor varies linearly to a maximum value of −0.496% as the hydrostatic pressure increases from 0.1 MPa to 15 MPa, with excellent consistency between the modeling (the blue plot) and experimental (the red plot) results. In addition, the FEA-predicted strain distributions of the circular pressure sensor under a hydrostatic pressure of 1–15 MPa, as shown in Fig. 3B, and Fig. S3 and S7 (ESI†), are more uniform compared with those of the rectangular pressure sensor due to the radially symmetric deformation in the sensor material caused by the hydrostatic pressure. Fig. 3C shows the fractional resistance change of the circular pressure sensor during the loading/unloading cyclic test (15 cycles, pressure range: 0.1 MPa–15 MPa), which indicates that the performance of this circular pressure sensor

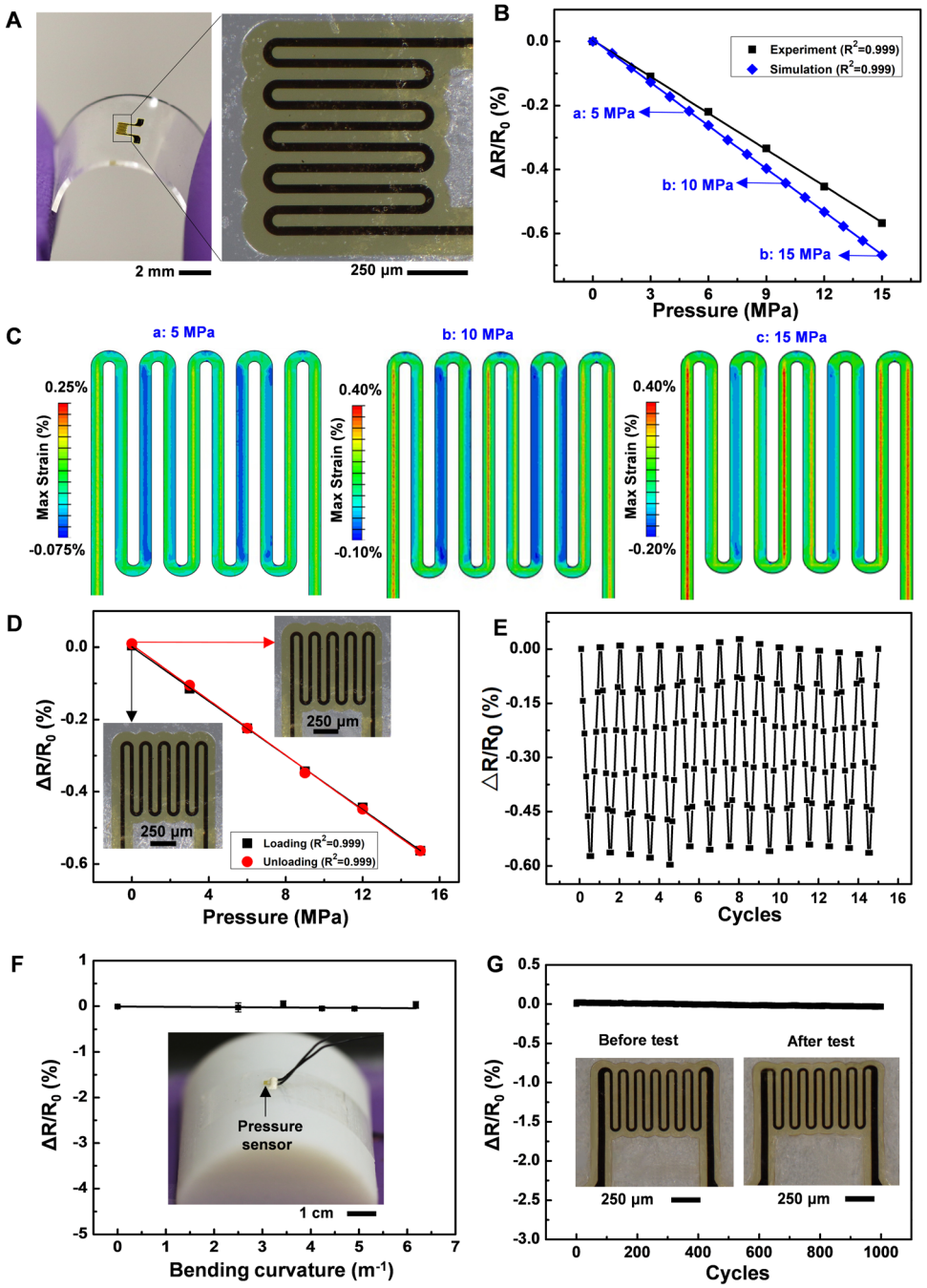

Fig. 2 Characterization of soft rectangular pressure sensors. (A) Optical images of the soft pressure sensor held by two hands. (B) Experimental and simulation results of the fractional resistance change of the rectangular pressure sensor as the hydrostatic pressure increases from 0.1 MPa to 15 MPa. (C) Finite element analysis of strain distributions in the pressure sensor under 5 MPa, 10 MPa, and 15 MPa, respectively. (D) Fractional resistance change of the pressure sensor under one cycle of loading/unloading in the hydrostatic pressure range of 0.1 MPa–15 MPa, with optical microscope images of the sensor before and after testing. (E) Cyclic loading test of the rectangular sensor. (F) Fractional resistance change of the pressure sensor as a function of bending curvatures (n = 3). (G) Fractional resistance change of the pressure sensor over 1000 cycles of a mechanical bending test.

is highly repeatable and reliable. The comparison between optical microscope images before and after testing in Fig. S4 (ESI†) also demonstrates that there is no significant change in the morphology of the sensor after testing. In addition, the cyclic bending test results of the circular pressure sensor in Fig. 3D show the high stability of the sensor performance with a negligible hysteresis resistance change (0.0459%) during cyclic bending tests (1000 cycles). Here, R_0 is the resistance of the pressure sensor before the cyclic bending test (under zero loading). We further design a pressure sensor with spike patterns of narrower Au traces (width: 34 μm), which has shown a resistance change of 0.439% over a pressure range of

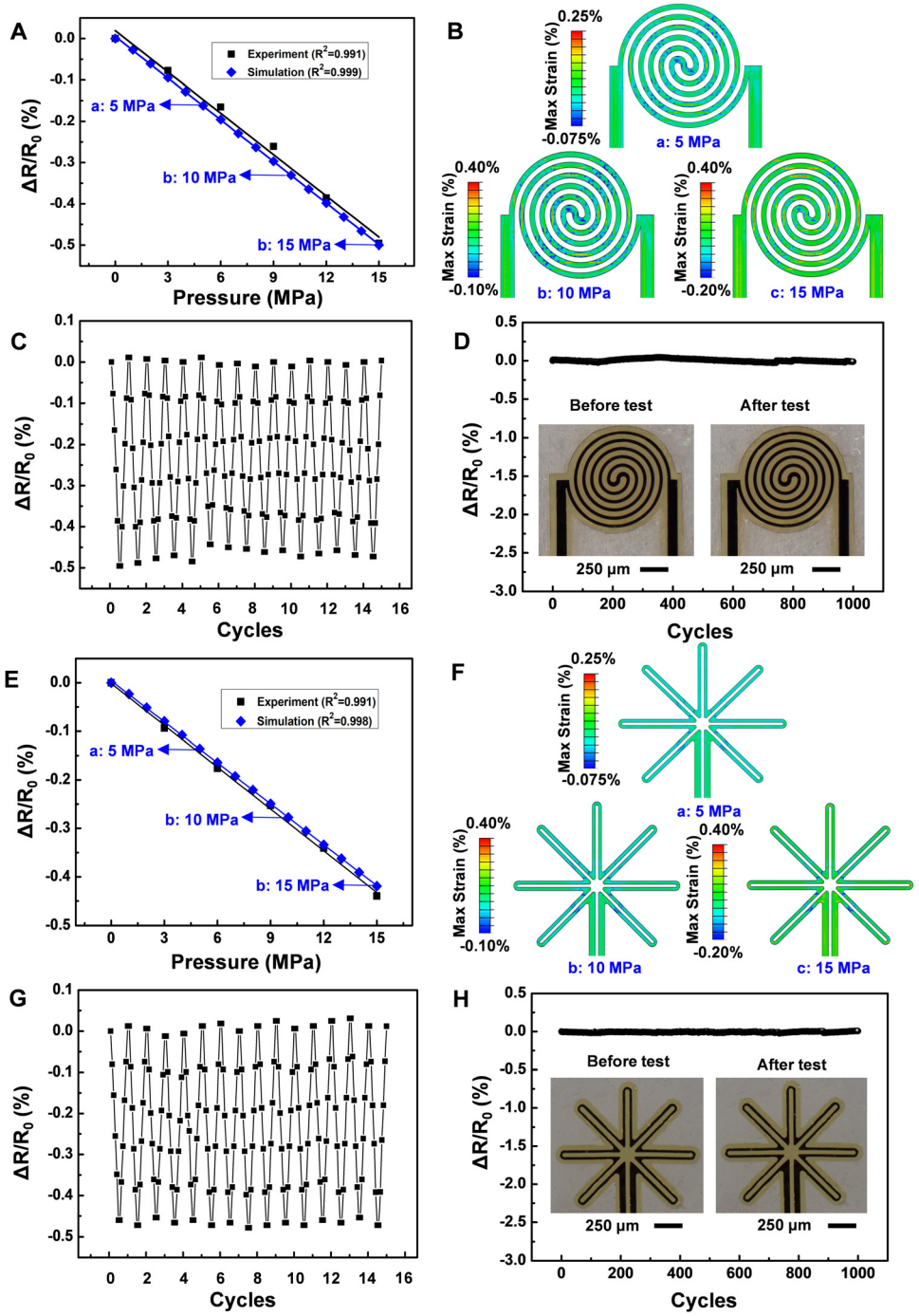

Fig. 3 Effect of sensor geometry on the performance of the pressure sensor. (A and E) Experimental and simulation results of the fractional resistance change of circular (A) and spike-shaped (E) sensors under hydrostatic pressures of 0.1–15 MPa. (B and F) FEA prediction of strain distributions within the circular (B) and spike-shaped (F) pressure sensors under 5 MPa, 10 MPa and 15 MPa, respectively. (C and G) Cyclic loading/unloading tests of the circular (C) and spike-shaped (G) pressure sensors. (D and F) Cyclic bending test of the circular (D) and spike-shaped (F) pressure sensors over 1000 cycles, with corresponding optical microscope images of the sensor before and after the test.

0.1 MPa–15 MPa (Fig. 3E). The experimental plot also shows excellent consistency with simulation results, where strain distributions of the radially symmetric spike-shape pressure sensor (Fig. 3F and Fig.S6 and S7, ESI†) remain relatively uniform as the pressure increases from 0.1 MPa to 15 MPa. In addition, the spike-shaped pressure sensor also exhibits high reliability and repeatability under cyclic loading (Fig. 3G and Fig. S8, ESI†) and bending tests (Fig. 3H), with no visible morphological changes after the cyclic and bending tests. In particular, Fig. 3H shows a negligible hysteresis resistance change of 0.0263%, where R_0 is the resistance of the pressure sensor before cyclic bending. These results demonstrate that

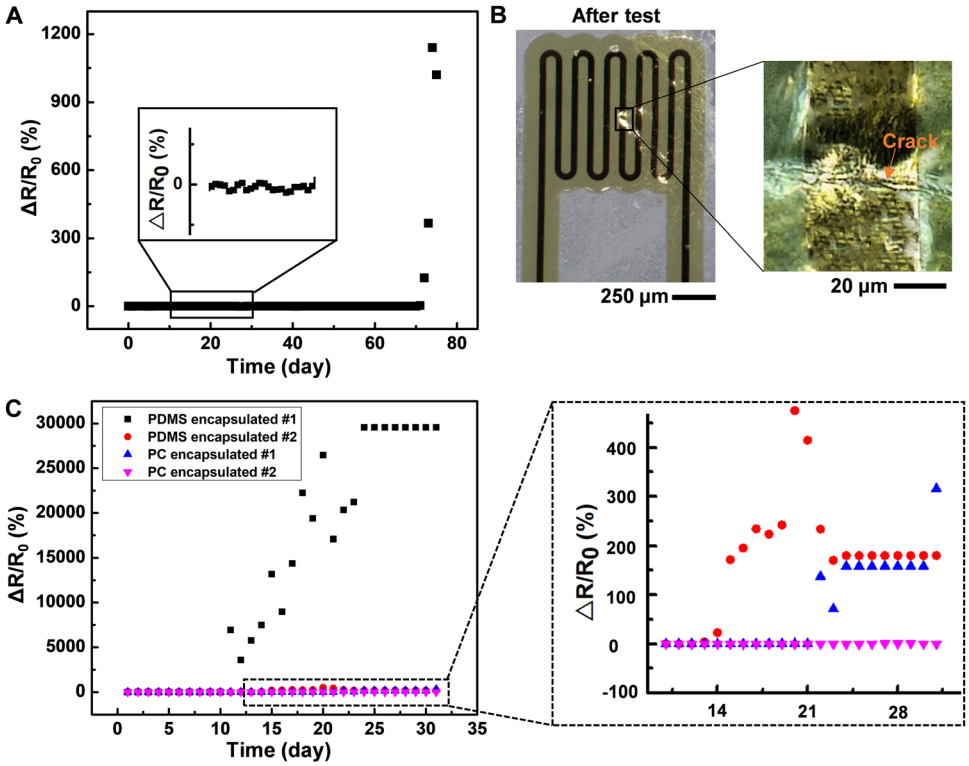

Fig. 4 Encapsulation capability of the soft pressure sensor. (A) Fractional resistance change of the rectangular pressure sensor tested under a hydrostatic pressure of 10 MPa in the pressure vessel filled with DI water. (B) Optical microscope images of the rectangular sensor after the test. (C) Comparison between the encapsulation capabilities of the PDMS film and Parylene C film for pressure sensors under 35 PSU salinity level and 10 MPa hydrostatic pressure conditions in the pressure vessel.

the two types of pressure sensors in radially symmetric geometry provide more uniform strain distributions under large hydrostatic pressures and, therefore, are potentially more mechanical robust for measuring a wide range of hydrostatic pressures in the ocean environment.

2.4 Encapsulation of pressure sensors for ocean sensing

As mentioned earlier, a Parylene C layer is coated on the fabricated resistive pressure sensor to improve the encapsulation capability, especially in harsh ocean environments. Fig. 4A presents the fractional resistance change of a rectangular pressure sensor that is encapsulated with Parylene C (6 μm), and its performance is monitored in the pressure vessel filled with deionized (DI) water under a hydrostatic pressure of 10 MPa. The sensor has negligible resistance changes over 72 days, which shows the excellent encapsulation capability of the Parylene C layer for operation under large hydrostatic pressures. The optical microscope image of the sensor after testing in Fig. 4B shows that the damage of the sensor beyond 72 days is probably caused by cracking in Au traces. To further evaluate the encapsulation capability of the Parylene C layer in the salinity environment, we test pressure sensors encapsulated with Parylene C and PDMS (for the control study), respectively, in 35 PSU NaCl solution in the pressure vessel (10 MPa) to monitor their performance. PDMS-encapsulated sensors are used for control studies here because PDMS has been widely used in the encapsulation of flexible electronics as wearable or implantable devices, due to its thermal and electrical insulation capability and biocompatibility.[50–52] Fig. 4C shows that the resistance of the two PDMS-encapsulated pressure sensors starts to increase abruptly on day 9 and day 14, respectively, while the Parylene C-encapsulated pressure sensor can maintain stable performance for up to 21 days (see Fig. 4D). The results demonstrate that the Parylene C-coated pressure sensor has a significantly improved encapsulation capability.

3. Conclusions

To sum up, the integrated experimental and simulation study on the developed soft, flexible pressure sensors reveals reliable sensor performance for sensing under large hydrostatic pressure and harsh ocean environments. Fabricated from ultra-thin gold films, the pressure sensors exhibit high linearity in resistance changes under a pressure increase from 0.1 MPa to 15 MPa. In addition, there is negligible hysteresis during the cyclic loading/unloading test of the sensor, and high flexibility is demonstrated during the cyclic bending test of up to 1000 cycles of the sensor. Pressure sensors of radially symmetric geometries enable more uniform strain distributions under large hydrostatic pressures compared to those of bilaterally symmetric geometries and therefore are more promising for measuring a wider range of hydrostatic pressures.

Furthermore, a thin Parylene C layer offers improved encapsulation capability of the pressure sensor, which has stable performance for up to 72 days under a large hydrostatic pressure of 10 MPa. The developed soft, flexible pressure sensor, along with other types of physical and chemical sensors,[33] has the potential to be integrated with various platforms like soft robotics[53] and diver equipment for sensing under harsh ocean conditions.

4. Experimental section

4.1 Design and fabrication of soft pressure sensors

A thin layer of poly(methyl methacrylate) (PMMA), which served as a sacrificial layer for the subsequent transfer printing of the sensor, was first spin-coated onto a cleaned glass slide. Then, the PMMA-coated slide was spin-coated (2000 rpm, 60 s) with a layer of liquid polyimide, which was then pre-heated at 130 °C for 5 minutes, followed by heating at 245 °C for 70 minutes in a PI oven (YES-58 HMDS Oven, Yield Engineering Systems Inc.) to obtain a 4 μm thick PI film. After this, magnetron sputtering (AJA Orion-8 Magnetron Sputtering System, AJA International Inc.) was used to deposit a thin layer of Cr (10 nm) and Au (100 nm) on PI, followed by photolithography and wet etching to pattern the Au/Cr layer into desired geometries of pressure sensors. Finally, another thin PI film (4 μm) was coated onto the patterned geometries to complete the microfabrication process.

4.2 Encapsulation with Parylene C

9 g Parylene C raw material was applied to coat a Parylene C film (6 μm) on the pressure sensor fabricated in section 4.1 *via* a Parylene C coater (Specialty Coating Systems Inc.). More specifically, pressure sensors were first placed in the deposition chamber of the Parylene C coater and the chamber was set under vacuum conditions. Raw Parylene C materials were added to the combustion chamber and the temperature was increased to 690 °C to vaporize the raw Parylene C material, which was uniformly deposited onto the surface of the sensors.

4.3 Cyclic loading/unloading tests of pressure sensors

To test the performance of the pressure sensor under various pressure levels, we utilized a pressure vessel (maximum pressure: 3000 psi; Pharr Instrument Company, Moline, IL) to perform cyclic loading/unloading tests (15 cycles) in the pressure range from 0.1 to 15 MPa. A syringe pump was used to increase/decrease the amount of water in the vessel, and a pressure controller was used to control the water flow between the pump and the vessel, thereby adjusting the pressure inside the vessel. The pressure inside the vessel is monitored *via* a pressure gauge installed on the head of the vessel, as shown in Fig. S9 (ESI†). The encapsulated pressure sensor was placed inside the vessel that was filled with deionized (DI) water and then the test was started. To enable the recording of the testing data, two wires were soldered onto the two contact pads of the pressure sensor and then connected to data acquisition equipment through the vessel head. Epoxy (Gorilla 4200101-2 Epoxy, Gorilla USA) was used for the encapsulation of connection wires. For each individual loading/unloading test cycle between 0.1 MPa and 15 MPa, when the inside pressure of the vessel reached the pre-set values (0.1 MPa, 3 MPa, 6 MPa, 9 MPa, 12 MPa, and 15 MPa, respectively) and remained stable, a multimeter was used to record the corresponding resistance of the pressure sensor.

4.4 Bending test of pressure sensors

To perform the bending test, we first utilized a 3D printer to fabricate 6 arched molds made of digital ABS, with bending curvatures of 0, 2.50 m^{-1}, 3.43 m^{-1}, 4.24 m^{-1}, 4.91 m^{-1}, and 6.18 m^{-1}, respectively. The pressure sensor was conformally laminated onto the arched mold *via* a thin double-sided tape. A multimeter was used to record the resistance of the sensor under various bending curvatures. The cyclic bending test was performed using a mechanical tester (CellScale, Univert) at a loading rate of 0.5 mm s^{-1} at room temperature. In an individual test cycle (Fig. 2G), the pressure sensor was held by two holders and bent at an angle of 40° and then recovered its flat state. A digital multimeter was used to record the resistance change of the sensor before and after each cycle.

4.5 Test of the encapsulation capability of the Parylene C film for pressure sensors

A low-temperature solder paste (Indium Corporation) was first applied on the contact pads of the pressure sensor, and two silicone-insulated copper wires (36 AWG, 25/50 BC, Calmont Wire and Cable) were then soldered on the contact pads, followed by the encapsulation of the soldering areas by marine epoxy (Loctite marine epoxy, Henkel Corporation). Subsequently, a Parylene C film was deposited onto the sensor. The encapsulated sensors were then tested inside the pressure vessel filled with DI water (hydrostatic pressure of 10 MPa), with their resistance values recorded once per day. To compare the encapsulation capability of the Parylene C film (6 μm) and the pure PDMS film (100 μm), pressure sensors encapsulated with Parylene C and PDMS films were placed in a plastic bellow that was filled with 35 PSU NaCl solution. The bellow was then placed in the pressure vessel filled with DI water (to minimize the contamination and potential corrosion of the pressure vessel) to test the performance of the pressure sensor under 10 MPa hydrostatic pressure and salinity environments. A multimeter was used to record the resistance values of the sensors once per day.

4.6 Modeling

A 3D finite element model was used to compare the effects of hydrostatic pressure on a variety of sensor shapes and sizes to identify the ideal sensor design to maximize the resistance change and the measurement range without inducing plastic deformation in the Au component of the sensor. To this end, the model was used to determine the effect of hydrostatic pressure on the strain distributions in the gold layer of the resistive pressure sensor. More specifically, the change in the

resistance of the pressure sensor can be calculated using the maximum strain of the gold layer of the device by relating the applied strain to the gauge factor of the material as follows:[54] where ρ is the resistivity of the material, l is the length of the unit segment, and a is the unit area.

$$R = \rho \frac{l}{a}. \quad (1)$$

Thus

$$\frac{dR}{R} = \frac{d\rho}{\rho} + \frac{dl}{l} - \frac{da}{a}. \quad (2)$$

In (2), we have

$$\frac{d\rho}{\rho} = C\frac{dV}{V}, \quad (3)$$

where C is Bridgman's constant, a material property that determines the thermodynamic change in resistivity,[55] and V is the unit volume. Therefore

$$\frac{dR}{R} = \frac{dl}{l}[C(1-2v) + 1 + 2v] = G\frac{dl}{l}, \quad (4)$$

and

$$\frac{R}{R_0} = (1 + G\varepsilon), \quad (5)$$

where G is the gauge factor of the material, which is shown to depend on Bridgman's constant and Poisson's ratio of the material, and ε is the strain in the material. The gauge factor of gold thin films is reported to be between 1.5 and 2.6, depending on factors such as the deposition method and grain size.[56] Thus, the change in the resistance of the sensor depends primarily on the gauge factor of the sensing material and the maximum strain that is applied to it, based on eqn (5). For this analysis, the maximum principal strain on the nodes (in Abaqus) that correspond to the Au layer of the sensor and a nanocrystalline Au thin-film with a gauge factor of 1.5[56] were used to determine an approximate change in the resistance of the sensor. The results from the simulation indicate that different sensor shapes (rectangular, circular, and spike) can survive hydrostatic pressures of up to 15 MPa before plastic deformation, which is expected at around 0.53% strain for Au thin films,[56] occurs in the sensor. The effects of the loading rate could not be adequately captured within the scope of this simulation, but the simulation and experimental results agree well overall. Experimental characterizations of the gauge factor and the maximum elastic strain of the Au thin film used in this study could improve the accuracy of the simulation by informing the conversion between the deformation strain and the resistance change of the pressure sensor under hydrostatic pressures.

Conflicts of interest

The authors declare no competing financial interests.

Acknowledgements

Y. L. S. H. L. and X. J. W. would like to acknowledge the support from the Office of Naval Research (N00014-19-1-2688 and N00014-21-1-2342). J. X. acknowledges the support from the National Science Foundation (CMMI-1762324). In addition, this work made use of the maskless aligner μMLA, which was funded by the Defense University Research Instrumentation Program from the Office of Naval Research (N00014-21-1-2223).

References

1 Z. Lou, S. Chen, L. Wang, K. Jiang and G. Shen, *Nano Energy*, 2016, **23**, 7–14.
2 J. Wang, Y. Zhu, Z. Wu, Y. Zhang, J. Lin, T. Chen, H. Liu, F. Wang and L. Sun, *Microsyst. Nanoeng.*, 2022, **8**, 16.
3 F. Xu, X. Li, Y. Shi, L. Li, W. Wang, L. He and R. Liu, *Micromachines*, 2018, **9**, 580.
4 R. A. S. I. Subad, L. B. Cross and K. Park, *Appl. Mech.*, 2021, **2**, 356–382.
5 Y. Cong, C. Gu, T. Zhang and Y. Gao, *Fundam. Res.*, 2021, **1**, 337–345.
6 S. Aracri, F. Giorgio-Serchi, G. Suaria, M. E. Sayed, M. P. Nemitz, S. Mahon and A. A. Stokes, *Soft Robotics*, 2021, **8**, 625–639.
7 J. M. Nassar, S. M. Khan, S. J. Velling, A. Diaz-Gaxiola, S. F. Shaikh, N. R. Geraldi, G. A. Torres Sevilla, C. M. Duarte and M. M. Hussain, *npj Flexible Electron.*, 2018, **2**, 1–9.
8 M. P. Johnson and P. L. Tyack, *IEEE J. Oceanic Eng.*, 2003, **28**, 3–12.
9 R. B. Mishra, N. El-Atab, A. M. Hussain and M. M. Hussain, *Adv. Mater. Technol.*, 2021, **6**, 2001023.
10 J. Jijesh, M. Susmitha, M. Bhanu and P. Sindhanakeri, *2017 2nd IEEE International Conference on Recent Trends in Electronics, Information & Communication Technology (RTEICT)*, IEEE, 2017, pp. 1487–1492.
11 M. Crescentini, M. Bennati and M. Tartagni, *AEU-Int. J. Electron. Commun.*, 2012, **66**, 630–635.
12 N. Brown, *OCEANS'87*, IEEE, 1987, pp. 280–286.
13 B. Lv, H.-l Liu, Y.-f Hu, C.-x Wu, J. Liu, H.-j He, J. Chen, J. Yuan, Z.-w Zhang and L. Cao, *Mar. Georesour. Geotechnol.*, 2021, **39**, 1044–1054.
14 R. Paradis and S. Wood, *2013 OCEANS-San Diego*, IEEE, 2013, pp. 1–12.
15 I. Anwar, M. O. Mohsin, S. Iqbal, Z. U. Abideen, A. U. Rehman and N. Ahmed, *2016 13th International Bhurban Conference on Applied Sciences and Technology (IBCAST)*, IEEE, 2016, pp. 547–553.
16 A. Bagheri, T. Karimi and N. Amanifard, *Appl. Soft Comput.*, 2010, **10**, 908–918.
17 J. Yuh and M. West, *Adv. Robot.*, 2001, **15**, 609–639.
18 W. Wang, J. Liu, G. Xie, L. Wen and J. Zhang, *Bioinspiration Biomimetics*, 2017, **12**, 036002.
19 D. B. Duraibabu, S. Poeggel, E. Omerdic, R. Capocci, E. Lewis, T. Newe, G. Leen, D. Toal and G. Dooly, *Sensors*, 2017, **17**, 406.

20 H. H. Gennerich and H. Villinger, *Earth Space Sci.*, 2015, **2**, 181–186.
21 X. Shuai, P. Zhu, W. Zeng, Y. Hu, X. Liang, Y. Zhang, R. Sun and C.-P. Wong, *ACS Appl. Mater. Interfaces*, 2017, **9**, 26314–26324.
22 Q. He, W. Zhang, T. Sheng, Z. Gong, Z. Dong, D. Zhang and Y. Jiang, *Flexible Printed Electron.*, 2022, **7**, 045002.
23 X. Sun, S. He, Z. Qin, J. Li and F. Yao, *Compos. Commun.*, 2021, **26**, 100784.
24 X. Sun, F. Yao and J. Li, *J. Mater. Chem. A*, 2020, **8**, 18605–18623.
25 G. Ge, Y. Zhang, J. Shao, W. Wang, W. Si, W. Huang and X. Dong, *Adv. Funct. Mater.*, 2018, **28**, 1802576.
26 A. G. Kottapalli, M. Asadnia, J. Miao, G. Barbastathis and M. S. Triantafyllou, *Smart Mater. Struct.*, 2012, **21**, 115030.
27 A. G. P. Kottapalli, C. W. Tan, J. Miao, G. Barbastathis and M. Triantafyllou, *2011 IEEE International Conference on Robotics and Biomimetics*, IEEE, 2011, pp. 1194–1199.
28 S. C. Mannsfeld, B. C. Tee, R. M. Stoltenberg, C. V. Chen, S. Barman, B. V. Muir, A. N. Sokolov, C. Reese and Z. Bao, *Nat. Mater.*, 2010, **9**, 859–864.
29 G.-W. Hsieh, S.-R. Ling, F.-T. Hung, P.-H. Kao and J.-B. Liu, *Nanoscale*, 2021, **13**, 6076–6086.
30 Y. S. Oh, J.-H. Kim, Z. Xie, S. Cho, H. Han, S. W. Jeon, M. Park, M. Namkoong, R. Avila and Z. Song, *Nat. Commun.*, 2021, **12**, 1–16.
31 S. Han, J. Kim, S. M. Won, Y. Ma, D. Kang, Z. Xie, K.-T. Lee, H. U. Chung, A. Banks and S. Min, *Sci. Transl. Med.*, 2018, **10**, eaan4950.
32 E. S. Hosseini, M. Chakraborty, J. Roe, Y. Petillot and R. S. Dahiya, *IEEE Sens. J.*, 2022, **22**, 9914–9921.
33 Y. Li, G. Wu, G. Song, S.-H. Lu, Z. Wang, H. Sun, Y. Zhang and X. Wang, *ACS Sens.*, 2022, **7**, 2400–2409.
34 S.-H. Lu, Y. Li and X. S. Wang, *J. Mater. Chem. B*, 2023, DOI: **10.1039/D3TB01167D**.
35 Y. H. Jung, Y. Qiu, S. Lee, T.-Y. Shih, Y. Xu, R. Xu, J. Lee, A. A. Schendel, W. Lin and J. C. Williams, *IEEE Antennas Wirel. Propag. Lett.*, 2015, **15**, 1382–1385.
36 C.-L. Chen, E. Lopez, Y.-J. Jung, S. Müftü, S. Selvarasah and M. R. Dokmeci, *Appl. Phys. Lett.*, 2008, **93**, 093109.
37 T. N. Chen, D. S. Wuu, C. C. Wu, C. C. Chiang, Y. P. Chen and R. H. Horng, *Plasma Processes Polym.*, 2007, **4**, 180–185.
38 X. Liu, Y. Zhu, M. W. Nomani, X. Wen, T.-Y. Hsia and G. Koley, *J. Micromech. Microeng.*, 2013, **23**, 025022.
39 D. Zeniieh, L. Ledernez and G. Urban, *Procedia Eng.*, 2014, **87**, 1398–1401.
40 W.-C. Kuo, T.-C. Wu, C.-F. Wu and W.-C. Wang, *Mater. Today Commun.*, 2021, **27**, 102306.
41 M. Sasaki, W. Xu, Y. Koga, Y. Okazawa, A. Wada, I. Shimizu and T. Niidome, *Materials*, 2022, **15**, 3132.
42 G. A. Bernier and D. E. Kline, *J. Appl. Polym. Sci.*, 1968, **12**, 593–604.
43 S. Wang, H. Zhou, G. Dang and C. Chen, *J. Polym. Sci., Part A: Polym. Chem.*, 2009, **47**, 2024–2031.
44 S. Numata and T. Miwa, *Polymer*, 1989, **30**, 1170–1174.
45 A. Al-Halhouli, I. Kampen, T. Krah and S. Büttgenbach, *Microelectron. Eng.*, 2008, **85**, 942–944.
46 M. Hopcroft, T. Kramer, G. Kim, K. Takashima, Y. Higo, D. Moore and J. Brugger, *Fatigue Fract. Eng. Mater. Struct.*, 2005, **28**, 735–742.
47 J. Gao, L. Guan and J. Chu, *6th International Symposium on Precision Engineering Measurements and Instrumentation*, SPIE, 2010, pp. 1578–1584.
48 M. Shaat and A. Abdelkefi, *J. Appl. Phys.*, 2016, **120**, 235104.
49 L. Wang and B. Prorok, *J. Mater. Res.*, 2008, **23**, 55–65.
50 I. Miranda, A. Souza, P. Sousa, J. Ribeiro, E. M. Castanheira, R. Lima and G. Minas, *J. Funct. Biomater.*, 2021, **13**, 2.
51 J. Oh, J.-H. Kim, S. Y. Lee, M. S. Kim, J. M. Kim, K. Park and Y.-S. Kim, *IEEE Trans. Device Mater. Reliab.*, 2017, **18**, 1–4.
52 Y. Zhang, D. Wen, M. Liu, Y. Li, Y. Lin, K. Cao, F. Yang and R. Chen, *Adv. Mater. Interfaces*, 2022, **9**, 2101857.
53 G. Li, X. Chen, F. Zhou, Y. Liang, Y. Xiao, X. Cao, Z. Zhang, M. Zhang, B. Wu, S. Yin, Y. Xu, H. Fan, Z. Chen, W. Song, W. Yang, B. Pan, J. Hou, W. Zou, S. He, X. Yang, G. Mao, Z. Jia, H. Zhou, T. Li, S. Qu, Z. Xu, Z. Huang, Y. Luo, T. Xie, J. Gu, S. Zhu and W. Yang, *Nature*, 2021, **591**, 66–71.
54 S. Zike and L. P. Mikkelsen, *Exp. Mech.*, 2014, **54**, 393–403.
55 P. W. Bridgman, *Phys. Rev.*, 1914, **3**, 273.
56 C. Li, P. Hesketh and G. Maclay, *J. Vac. Sci. Technol., A*, 1994, **12**, 813–819.